Morphological Characterization of Intracranial Aneurysms Using 3-D Moment Invariants

R. D. Millán, L. Dempere-Marco, J. M. Pozo, J. R. Cebral, and A. F. Frangi*, *Senior Member, IEEE*

Abstract—Rupture of intracranial saccular aneurysms is the most common cause of spontaneous subarachnoid hemorrhage, which has significant morbidity and mortality. Although there is still controversy regarding the decision on which unruptured aneurysms should be treated, this is based primarily on their size. Nonetheless, many large lesions do not rupture whereas some small ones do. It is commonly accepted that hemodynamical factors are important to better understand the natural history of cerebral aneurysms. However, it might not always be practical to carry out a detailed computational analysis of such factors if a prompt assessment is required. Since shape is likely to be dependent on the balance between hemodynamic forces and the aneurysmal surrounding environment, an appropriate morphological 3-D characterization is likely to provide a practical surrogate to quickly evaluate the risk of rupture. In this paper, an efficient and novel methodology for 3-D shape characterization of cerebral aneurysms is described. The aneurysms are isolated by taking into account a portion of their adjacent vessels. Two methods to characterize the morphology of the aneurysms models using moment invariants have been considered: geometrical moment invariants (GMI) and Zernike moment invariants (ZMI). The results have been validated in a database containing 53 patients with a total of 31 ruptured aneurysms and 24 unruptured aneurysms. It has been found that ZMI indices are more robust than GMI, and seem to provide a reliable way to discriminate between ruptured and unruptured aneurysms. Correct rupture prediction rates of $\simeq 80\%$ were achieved in contrast to 66% that is found when the aspect ratio index is considered.

Index Terms—Intracranial aneurysms, morphological characterization, 3-D Zernike moments.

I. INTRODUCTION

INTRACRANIAL aneurysms are pathological enlargements of brain arteries that are most commonly located at the Circle of Willis [1]. Due to the increasing use of modern imaging techniques, unruptured intracranial aneurysms (UIA) are detected more frequently than in the past. However, the natural history of UIA is still poorly understood. The reasons for genesis, growth, and rupture of saccular aneurysms are not clear [2], and the management of patients with UIA remains controversial [3], [4]. Subarachnoid hemorrhage (SAH) due to the rupture of an intracranial aneurysm is a devastating event associated with high rates of mortality (40%–50%) and morbidity [5]–[7]. The International Study of Unruptured Intracranial Aneurysms (ISUIA) Study Group undertook an epidemiological project in 1991, in order to gain a better understanding of the natural history of UIA and the risks associated with their surgical or endovascular repair [8], [9]. The objective of the ISUIA trial is to help in defining the optimal management of patients with UIA. It was concluded that size and location might play an important role in predicting rupture risk, especially in patients who have not had SAH previously. Low rupture rates (about 0.1% per year) were found in such cases for UIAs for diameters less than 7 mm. Although surgical or endovascular treatment of UIA may prevent SAH, both have also procedure-related risks. Thus, it is necessary to establish the risk–benefit ratio for these patients. Unfortunately, this is not always clear [9]. In fact, it has been argued whether there exists a critical threshold or, on the contrary, it is possible to derive a continuous risk score based on size information [3].

Hemodynamical factors, such as wall shear stress, pressure, residence time, and flow impingement, are thought to play a role in the pathogenesis of aneurysms and thrombosis [5], [10]. Measuring hemodynamic quantities *in vivo* is, however, difficult and involves significant patient risk. To tackle this problem, various modeling approaches have been considered in the past for characterizing and measuring hemodynamic quantities [11]. The main obstacle for applying computational methods to large numbers of patient-specific aneurysm geometries is the computational power required to perform the calculations in a timely manner. Typically, the segmentation and semi-automatic model preprocessing takes at least several hours, and the computational cost for full 3-D computational fluid dynamics (CFD) in current computers is of the order of one day. Thus, although CFD is important for a better understanding of the natural history of cerebral aneurysms, it might not always be practical to carry out such an analysis if a prompt assessment of whether a patient is at risk or not is needed. On the other hand, shape is likely both, to have major influence on the fluid dynamics and to be dependent, to some extent, on the balance between hemodynamic forces and the surrounding environment. Thus, it can be concluded that these methods provide complementary information. An appropriate morphological 3-D characterization may, however, provide a practical surrogate to quickly evaluate the risk

of rupture before fully resource demanding 3-D CFD analysis is performed. For the methodology presented here, the semi-automatic model preprocessing is lighter than for CFD, since shorter pieces of the adjacent vessels are needed, and the computational cost for obtaining the shape descriptors considered in this paper is around half an hour.

Nowadays, the shape index most commonly used to predict rupture is the largest diameter of the aneurysm. Nevertheless, this parameter alone does not suffice to explain the natural history of aneurysms leading to rupture [2], [9], [12], [13]. Cerebral saccular aneurysms show a substantial amount of variation in both shape and size, and reliable morphological indices for aneurysmal rupture have not been elucidated. Therefore, a more comprehensive quantitative description is necessary. Fortunately, with the current advances in medical imaging, it is now feasible to obtain 3-D reconstructions of cerebral aneurysms from computed tomography angiography (CTA), 3-D rotational angiography (3DRA), and magnetic resonance angiography (MRA). This offers the opportunity to analyze the anatomy of the aneurysm in all its complexity. However, to date there has been little work on detailed geometrical characterization of brain aneurysms and its connection to rupture risk [4], [14]–[16]. In 1999, Ujiie *et al.* [14], proposed the aspect ratio (aneurysm depth/neck width) as an indicator of rupture risk. The aspect ratio has been successfully used to single out small aneurysms with an associated high rupture risk. Despite being useful in some cases, it has been pointed out that the aspect ratio does not provide accurate predictions in general [17]–[19]. Ma *et al.* [15] recently proposed some parameters to characterize the 3-D aneurysm geometry. In a posterior work [16], the usefulness of these parameters to predict the rupture risk was studied. Although the results were promising, significant user interaction was required for the definition of such indices. Finally, Rohde *et al.* [4] analyzed the shape of 46 ruptured and 45 unruptured intracranial aneurysms for which 3DRA images were available. To that moment, qualitative assessments about the existence of surface irregularities had been considered for predicting rupture risk. The objective of this work was to introduce quantitative morphometric measures capable of encapsulating such shape irregularities. The first few coefficients of the 2D Fourier analysis from the manually delineated contours of the aneurysms were compared between the ruptured and unruptured sets. Such contours were defined on the projection plane showing the best relationship between aneurysm neck and parent vessel while preserving the maximal extension of the aneurysmal sac. This is similar to the *working projection* used for endovascular coiling. Although statistically significant differences were found for some of the coefficients, showing that morphological aspects may play a significant role in rupture risk assessment, the main drawbacks of this method are, on one hand, the highly subjective selection of the working projection plane, and more importantly, the fact that the analysis is limited to 2D contours rather than exploiting the full potential of the 3-D information.

It is thus necessary to investigate methods for characterizing complex 3-D shapes in an automatic fashion. To this end, moment theory has been considered in this work. Recently, geometric moment invariants have been utilized in medical image
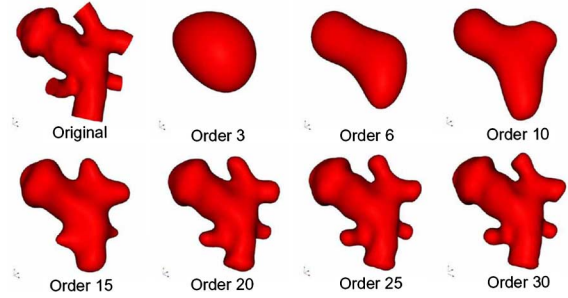

Fig. 1. Reconstruction of an aneurysm illustrated by isosurfaces of the reconstructed volumetric function. Upper left is the original object mesh. The number below each image indicates the order of Zernike moments that has been used for reconstruction.

analysis for studying brain morphometry [20]. In the present work, only indices invariant to similarity transformations (translation, scaling and rotation) are considered, i.e., geometric moment invariants (GMI) and Zernike moment invariants (ZMI). Both types of shape indices can be computed employing the classic geometric moments. Our proposed method computes the geometric moments by using the Divergence Theorem, thus allowing the calculation of shape indices of volumetric objects from their surface, which is represented by a nonstructured mesh of triangles.

The aim of this work is to provide a methodology to geometrically characterize 3-D shapes of cerebral saccular aneurysms using moment based descriptors. In Section II, a brief introduction to moment theory is presented, including a short description of both GMI and ZMI. A description of the data used in this study and several implementation issues are discussed in Section III. This is followed by an assessment of the robustness of the proposed methods in Section IV. This section also includes a series of experiments investigating the predictive value of the moment invariants regarding rupture events. Finally, Section V presents the conclusions and a detailed discussion of all the relevant issues addressed in this work.

II. MOMENT THEORY

The aim of this section is to provide a brief introduction to 3-D moment theory in the context of shape analysis.

A. General Theory

The use of moments in the context of shape analysis is described in [21]. Moments are defined as

$$m_i = \langle f, \psi_i \rangle = \int_\Omega f(\mathbf{x}) \cdot \overline{\psi_i(\mathbf{x})} \, d\mathbf{x} \tag{1}$$

where f is a square integrable object function, i.e., $f \in L^2$. Thus, the moments are projections onto a basis of functions $\Psi = \{\psi_i\}$ $(i \in \mathbb{N})$ over the domain Ω.

Two desirable properties of the basis of functions Ψ are completeness and orthonormality. They imply the capability to reconstruct the original object (see Fig. 1) from the moments m_i. The object is more accurately approximated by increasing the order K of moments until convergence to the original object is achieved at infinity.

In addition, a desirable property of a shape descriptor, based on moments or not, is the invariance under similarity transformations. Moments are not invariant in general, but some invariants can be derived from them.

B. 3-D Geometric Moment Invariants

Geometric moments have been previously utilized in medical image processing [20], [22] to construct invariants to similarity transformations, which can be used for automatic recognition of pathological deformations. Geometric moments are the basis for the computation of different kinds of moments, in particular Zernike moments. It is, therefore, necessary to ensure an accurate and efficient computation of the geometric moments. In this work, both volume-based moments and surface-based moments are considered.

Volume-Based Moments: The 3-D geometric moments of order K of a function $f(\mathbf{x})$ are defined in terms of the Riemann integral as [23]

$$m_{\mathrm{pqr}} = \int_{\Omega} f(\mathbf{x}) x^p y^q z^r \, d\mathbf{x} \qquad (2)$$

where $0 \leq p + q + r \leq K$, $0 \leq K < \infty$, and $\mathbf{x} \in \Omega \hookrightarrow \mathbb{R}^3$ denotes a vector $\mathbf{x} = (x, y, z)^T$. It is assumed that $f(\mathbf{x})$ is a piecewise continuous functions that can have nonzero values only in a finite region of $\mathbb{R}^3$, thus ensuring that moments of all order exist.

Geometric moments are generally calculated by using the object volume, and such calculations have an associated $\mathcal{O}(N^3)$ complexity. In 1997, Yang *et al.* [24] proposed a very fast algorithm that works over a structured mesh of squares in order to obtain geometric moments by using the Divergence Theorem. Unfortunately, this approach had a limiting voxel precision. In order to avoid this fact, in this work, geometric moments are computed via the divergence theorem in a nonstructured mesh of triangles (see Appendix A).

Scale invariance can be achieved by isometric scaling of the central moments [24]–[26]. The central moments are translation invariant, and are defined as

$$M_{\mathrm{pqr}} = \int_{\Omega} f(\mathbf{x})(x - x_0)^p (y - y_0)^q (z - z_0)^r \, d\mathbf{x} \qquad (3)$$

where (x_0, y_0, z_0) is a spatial point appropriately selected (e.g., the centroid or center of mass (CM) of the density function $f(\mathbf{x})$, or the bifurcation point (BP) of the object medial axis).

The central moments can be expressed in terms of the original moments, (2), by the formula [24], [25]

$$M_{\mathrm{pqr}} = \sum_{s=0}^{p} \sum_{t=0}^{q} \sum_{u=0}^{r} (-1)^k \binom{p}{s} \binom{q}{t}$$
$$\times \binom{r}{u} x_0^s y_0^t z_0^u m_{p-s, q-t, r-u} \qquad (4)$$

where $k = s + t + u$, and $\binom{m}{n} = (m!/(n!(m-n)!))$ is the binomial coefficient.

Then, the scale-invariant central moments are obtained as

$$\mu_{\mathrm{pqr}} = \frac{M_{\mathrm{pqr}}}{(M_{000})^{\gamma}}, \quad \gamma = \frac{p + q + r}{3} + 1. \qquad (5)$$

In contrast to translation and scale invariance, the computation of moments invariant to rotation is a time-consuming task. Here only the main steps of their calculation are outlined. The first systematic approach to the derivation of 3-D moment invariants to rotation was published in 1989 by Lo and Don [23]. They derived rotational invariants of order 2 and 3 by using group theory and tensor calculus. Rotation invariants stem from the finest possible decomposition leading to irreducible representations [27]. If a rotation is applied to a centered object, its moments of order K are transformed into linear combinations of the same order. Consequently, an object $f(\mathbf{x})$ can be decomposed as a direct sum of orthogonal subspaces, $\mathcal{E}_l$, each of which is globally invariant to rotation. If a vector belongs to $\mathcal{E}_l$, its image resulting from any rotation will also belong to $\mathcal{E}_l$. The basis corresponding to this decomposition is that of harmonic polynomials $y_l^m(\mathbf{x})$. The harmonic polynomials $y_l^m(\mathbf{x})$ are defined as

$$y_l^m(\mathbf{x}) = r^l Y_l^m(\boldsymbol{\xi}) \qquad (6)$$

where $l \leq K$, $-l \leq m \leq l$, and $Y_l^m(\boldsymbol{\xi})$ are the spherical harmonics. Then, in the basis of spherical harmonics, the rotational operator becomes irreducible and corresponds to a block-diagonal matrix. In the new basis, the geometric moments are transformed into complex moments ν_l^m, where m is a tensor index, and rotation invariants can be derived from tensor contraction [23], [27], [28].

Rotation invariants are inferred from all the possible applications of the tensor product to ν_0^m, ν_1^m, ν_2^m, and ν_3^m yielding scalars which are the 3-D moment invariants. Therefore, the geometric moment invariants are homogeneous polynomials of scale-invariant moments. Because of symmetries, the tensor contraction leads to only 12 invariants, denoted by I_β^α, where α is the order of the moments and β is the orthogonal subspace index (i.e., index of the $\mathcal{E}_l$). Finally, the GMI are reduced [28], [29] through normalization, and hence, each reduced moment invariant becomes

$$\tilde{I}_\beta^\alpha = \mathrm{sign}\left(I_\beta^\alpha\right) \cdot \left|I_\beta^\alpha\right|^{1/d} \qquad (7)$$

where d is the polynomial degree of the invariant.

Surface-Based Moments: GMI are defined from surface geometric moments in a straightforward manner, by following the same steps that in the volume-based GMI. While for volume-based moments the density function representing the object has support in the interior, being set to 0 in the exterior of the object, for surface-based moments the density function has support only on the surface, being 0 in both the interior and the exterior. It can be defined as

$$f(\mathbf{x}) = g(\mathbf{x}_{\partial\Omega})\delta(\mathbf{x} - \mathbf{x}_{\partial\Omega}) \qquad (8)$$

where $g(\mathbf{x})$ is a piecewise continuous and bounded function defined on the object surface, and $\delta(\mathbf{x} - \mathbf{x}_{\partial\Omega})$ is the Dirac delta function. Therefore, surface geometric moments are calculated as

$$m^S_{\mathrm{pqr}} = \int_{\partial\Omega} g(\mathbf{x}) x^p y^q z^r \, d\sigma. \qquad (9)$$

Translation invariance could be obtained by using (3) or (4), to achieve scale invariance. However, for surface moments, (5) must be modified such that the parameter $\gamma = ((p+q+r)/2)+1$. Finally, rotation invariant surface GM are obtained by applying the same methodology presented for volume-based GMI [23], [28], [29], see (6) and (7).

C. 3-D Zernike Moment Invariants

Zernike moments were selected because they have demonstrated a good performance with regard to noise resilience, information redundancy and reconstruction capability [30], [31]. Zernike moments are derived from the Zernike polynomials, which in 3-D are defined as $Z^m_{nl}(\mathbf{x})$ [21], [32]

$$Z^m_{nl}(\mathbf{x}) = R_{nl}(r) Y^m_l(\boldsymbol{\xi}) \qquad (10)$$

where $Y^m_l(\boldsymbol{\xi})$ are the spherical harmonics of lth degree orthonormal on the surface of the unit sphere with $l \leq n$, while m ranges from $-l$ to l, and $n - l$ is an even, nonnegative integer. $R_{nl}(r)$ is a real factor depending on the radius r so that $Z^m_{nl}(\mathbf{x})$ become a set of polynomials orthonormal within of the unit sphere.

The 3-D Zernike moments Ω^m_{nl} of an object defined by $f(\mathbf{x})$ are

$$\Omega^m_{nl} = \langle f(\mathbf{x}), Z^m_{nl}(\mathbf{x}) \rangle = \frac{3}{4\pi} \int_{|\mathbf{x}| \leq 1} f(\mathbf{x}) \overline{Z^m_{nl}(\mathbf{x})} \, d\mathbf{x}. \qquad (11)$$

It is important to notice that the 3-D Zernike moments Ω^m_{nl} are not invariant under rotations. This means that if the same aneurysm model is represented in a rotated reference frame, the Zernike moments computed from the transformed model, $(\Omega^m_{nl})'$, will have different values, $(\Omega^m_{nl})' \neq \Omega^m_{nl}$. In order to achieve the desirable invariance with respect to the reference orientation, the approach followed in [21] is applied. The moments are collected into $(2l+1)$-dimensional vectors $\boldsymbol{\Omega}_{nl} = (\Omega^l_{nl}, \Omega^{l-1}_{nl}, \ldots, \Omega^{-l}_{nl})^T$ and the rotationally invariant 3-D Zernike descriptors F_{nl} are obtained as the norms of the vectors $\boldsymbol{\Omega}_{nl}$

$$F_{nl} = \|\boldsymbol{\Omega}_{nl}\|. \qquad (12)$$

Translational invariance is achieved by shifting the (x_0, y_0, z_0) point in (3) into the origin. Scale invariance can be achieved by scaling the object in such a way that some geometric parameter characterizing its extension is fixed to some value. For the computation of the Zernike moments it is necessary that the object is circumscribed within the unit

sphere. Thus, the most simple election would be to fix the radius from the center to the farthest object point to a unitary length, $R = 1$. This provides the best resolution power for characterizing the shape by ZMI. However, this simple scaling is too sensitive to the determination of the vessels cut plane and the center position. To avoid this problem, Novotni and Klein introduced in [33] a better normalization by fixing the object spread to $1/2$. No fixed value for the spread can mathematically guaranty that any shape will fit inside the unit sphere. But a value can be chosen experimentally, for which it is likely that any object of the expected shape range will fit inside the unit sphere. For the scaling of the isolated aneurysms, we have used this spread-based normalization method. The maximum spread value for which all the objects of the dataset has radius $R \leq 1$ was computed and the scaling spread value was chosen to be 0.99 of such maximum.[1] This is a convenient selection for our data set to illustrate the potential of the described methodology. Nonetheless, in order to implement it in a larger training set for rupture risk estimation of previously unseen test aneurysms, an appropriate margin should be decided in terms of the expected spreads, thus guaranteeing that virtually (say with a 99.9% probability) any new aneurysm will fit inside the unit sphere. The possible exclusion of some aneurysms is highly compensated by the gaining in robustness against cut-plane selection and segmentation method. Moreover, the excluded aneurysms would indeed have an extremely elongated shape, which, according to current clinical practices, would make them a very probable candidate to be treated.

It can be shown [21], [32] that Zernike moments Ω^m_{nl} can be written as a linear combination of geometric moments of up to order n

$$\Omega^m_{nl} = \frac{3}{4\pi} \sum_{r+s+t \leq n} \chi^{\mathrm{rst}}_{\mathrm{nlm}} M_{\mathrm{rst}}, \qquad (13)$$

where M_{rst} denotes the geometrical central moment of the object normalized to fit in the unit ball, and $\chi^{\mathrm{rst}}_{\mathrm{nlm}}$ are complex coefficients.

Since the functions Z^m_{nl} form a complete orthonormal system, it is possible to approximate the original function f by a finite number of 3-D Zernike moments Ω^m_{nl}

$$\hat{f}(\mathbf{x}) = \sum_{n=0}^{K} \sum_{l=0}^{n} \sum_{m=-l}^{l} \Omega^m_{nl} Z^m_{nl}(\mathbf{x}). \qquad (14)$$

Here, the sum is performed over $n \in [0, K]$, $l \in [0, n]$ such that $n - l$ is an even number and $m \in [-l, l]$. The reconstruction can be used to verify how much of the original object information is included in a set of 3-D Zernike moments up to a given order $n = K$ (see Fig. 1). This can be intuitively understood by considering that the spherical harmonics (SH) can be interpreted as a Fourier basis on the sphere, i.e., this part of the basis functions measures the angular frequencies of the object. By further considering the product with the radial polynomials, it can

---

[1]The spread values obtained from our dataset for the four types of ZMI considered, $\mathrm{Volume_{CM}}$, $\mathrm{Volume_{BP}}$, $\mathrm{Surface_{CM}}$, and $\mathrm{Surface_{BP}}$, are 0.187, 0.212, 0.287, and 0.257, respectively.

TABLE I

CLASSIFICATION OF THE PATIENT DATA SET ACCORDING TO LOCATION, WHERE n IS THE NUMBER OF CASES PER CLASS. THE MEAN SIZE OF THE MAXIMUM ANEURYSMAL DOME AND ITS ASSOCIATED STANDARD DEVIATION ARE ALSO PRESENTED

	n	size [mm]
ACoA	8	4.0 ± 1.0
PCoA	15	9.9 ± 4.7
MCA	18	9.7 ± 7.2
ICA	19	7.1 ± 4.4
SCA	1	12.0 ± 0.5
VA	3	9.3 ± 5.0
basilar	1	4.0 ± 0.5

TABLE II

ANEURYSM TYPES IN THE DATABASE ANALYZED. R AND U DENOTE RUPTURED AND UNRUPTURED ANEURYSMS, RESPECTIVELY. ANEURYSMS HAVE ALSO BEEN CLASSIFIED ACCORDING TO THE TYPE OF CLINICAL TREATMENT UNDERGONE (I.E., COIL OR CLIP). LAST COLUMN SUMMARIZES THE NUMBERS OF CASES UTILIZED IN THIS STUDY

	Database		With Coil		With Clip		Utile	
	R	U	R	U	R	U	R	U
Lateral	9	14	2	-	-	-	7	14
Bifurcation	13	3	1	-	-	-	12	3
Terminal	12	9	-	1	-	1	12	7
Fusiform	1	2	-	-	-	-	-	-
	35	28	3	1	-	1	31	24

be seen that different moments measure different frequencies of the object in the radial direction.

Surface-Based Zernike Moment Invariants: The computation of surface-based ZMI is completely analogous to volume-based ZMI. It is only necessary to compute central moments, (4), by using the surfaced-based geometric moments from (9), and to change the factor $3/(4\pi)$ by the factor $1/(4\pi)$ in (11) and (13).

Geometric and Zernike moments have been presented for a general volume-based, $f(\mathbf{x})$, or surface-based, $g(\mathbf{x})$, density function. However, for the methodology presented here, only homogeneous density functions will be considered: $f(\mathbf{x}) = 1$ or $g(\mathbf{x}) = 1$ on the corresponding support. This means giving the same weight to all parts of the object. Thus, for instance, the two types of geometric moments will be

$$ m_{\mathrm{pqr}}^{\mathrm{V}} = \int_\Omega x^p y^q z^r \, d\mathbf{x} \quad \text{and} \quad m_{\mathrm{pqr}}^{\mathrm{S}} = \int_{\partial\Omega} x^p y^q z^r \, d\sigma $$

where Ω denotes the interior of the object and $\partial\Omega$ its surface.

III. MATERIALS AND METHODS

A. Data Description

The clinical data sets consist of 12 brain aneurysms derived from CTA imaging studies and 51 aneurysms obtained from 3DRA imaging studies corresponding to 53 patients. Most aneurysms appear at the Circle of Willis, more specifically, in the following locations: anterior communicant (ACoA), posterior communicant (PCoA), middle cerebral (MCA), internal carotid (ICA), superior cerebelar (SCA), vertebral (VA), and basilar arteries. Table I shows the distribution of the cases according to their location, and the mean values of the maximum dome size derived from manual measurements on the images along with their associated standard deviations.

Additionally, patient information indicating which aneurysms presented SAH before the scan was done was also available (Table II). It should be pointed out that, since aneurysm shape is inherently related to hemodynamic forces and the surrounding environment, and the objective of both surgical procedures (i.e., clipping) and endovascular treatments (i.e., coils or stents) is to alter the blood flow, those aneurysms which have already undergone any of these treatments have not been considered in this study. Furthermore, it is also common to classify the aneurysms according to their location with respect to the parent artery: lateral, bifurcation, terminal, and fusiform aneurysms [34]. This classification conveys more information

regarding the flow and will be used in this study. Fusiform aneurysms were not considered either since their pathogenesis is clearly different from that of saccular aneurysms.

Image acquisition in the CTA data base was performed by using an Helical Elscint CT Twin scanner (Marconi; Haifa, Israel) with 120 kV/300 mA for the amplifier tube, 1.2-mm collimation with an helical pitch of 1 and slice spacing of 0.65 mm. Images were reconstructed on a 512×512 matrix with a square field-of-view (FOV) of 20.8 cm yielding an in-plane resolution of 0.4 mm.

The 3DRA catheter angiograms were performed by standard transfemoral catheterizations of the cerebral vessels and digital subtraction imaging done on a Philips Integris Biplane Unit (Philips Medical Systems, Best, The Netherlands). Rotational angiograms were performed using a 6-s constant injection of contrast agent and a $180°$ rotation with imaging at 15 frames per second over 8 s for acquisition of 120 images. Data from these images were transferred to the Philips Integris Workstation and reconstructed into 3-D voxel data using the standard proprietary software. The image data consist of $128 \times 128 \times 128$ voxels, with 16 bits per voxel, and a FOV of 54.04 mm, thus leading to a voxel size of 0.42 mm.

The typical sizes of arteries are 5 mm for ICA and 3 mm for MCA, and the average of the aneurysms size in our data set is around 8 mm (see Table I). Thus, the spatial resolution of these imaging systems enables a good characterization of the geometry of the aneurysms. However, some sensitivity of the shape descriptors to the segmentation accuracy is not discardable *a priori*. In order to determine, to some extent, the importance of this sensitivity, an experiment comparing the different models obtained from two segmentation methods has been conducted. It is furthermore expected that with the advent of new technological advances, an improvement in spatial resolution will follow and more subtle variations will therefore be detected.

B. Segmentation Methods

Moment invariants are calculated by using the triangular mesh derived from the segmented models of the aneurysms. Two alternative approaches were used for the segmentation depending on the image modality. For the 3DRA images, a *deformable surface model* method [35], [36] was applied. The optimized parameters were set as described in [35]. For the CTA images, a *region-based implicit deformable surface* method was employed. The selection of optimal parameters was done as described in [37]. A 3-D model of the aneurysm
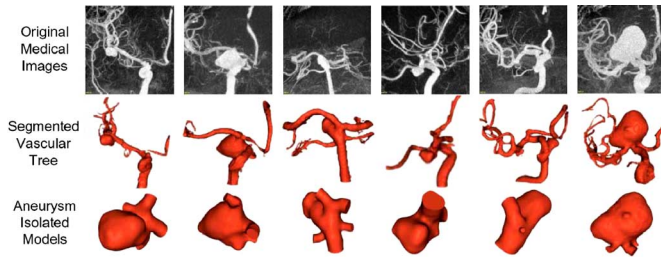
Fig. 2. Three-dimensional image-based aneurysm models. Top row: original 3-D X-ray angiograms. Middle row: segmented vascular tree. Bottom row: isolated aneurysm models.
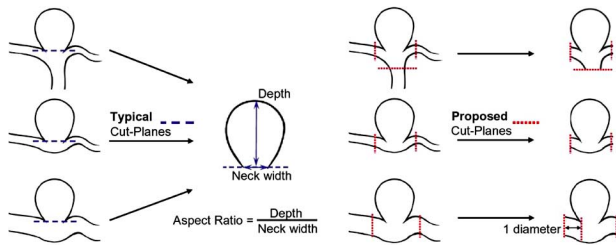

Fig. 3. Comparison of the common and proposed procedures for isolating aneurysm models. By keeping a portion of the adjacent vessels, different cases with identical domes provide distinct models.
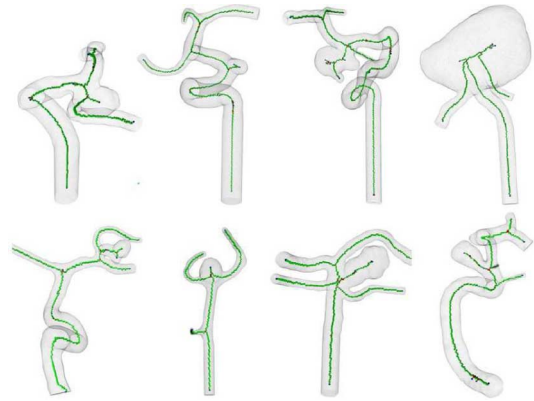

Fig. 4. Different arterial trees of real cases and their skeletons. Meaning of the colors is as follows: red are bifurcation voxels, green are simple voxels, and blue are terminal voxels.

was reconstructed from the segmentation results by using the marching cubes algorithm with a grid resolution between 0.1 and 0.2 mm. The reconstructed surface was then smoothed by using a non-shrinking algorithm [38], and the triangulation was optimized by using edge collapsing and diagonal swapping [39]. The anatomical aneurysm model was then used as a support surface to generate a uniform triangular mesh surface [40], varying from 50 000 to 120 000 elements.

C. Isolation of Aneurysm Models

The aneurysmal models were defined by cutting the parent vessels at a distance of approximately one diameter of the corresponding vessel from the aneurysm neck (see Fig. 2). Such a criterion was empirically selected with the objective of including information about the parent vessels for better characterizing flow dependent effects, while not changing considerably the overall shape of the models. As illustrated in Fig. 3, the consideration of a portion of the parent vessels makes it possible to distinguish different models with identical aneurysmal dome. By using the ordinary method to characterize their shape, all of the models would have the same morphological characteristics, while their rupture risk is arguably different.

Furthermore, in order to obtain translation invariance, it is necessary to select a point of the model for centering all the models in a common way. Both the bifurcation point and the center of mass of the aneurysm models have been selected for such purpose and their results are compared.

D. Skeleton Extraction

After isolating the models, it is necessary to normalize such models for computing the global shape features. This normalization is obtained by applying the Euclidean pose transforma-

tions: translation, scaling, and rotation. To obtain translation invariance, most approaches translate the CM of the object into the origin. As mentioned earlier, another way to achieve translation invariance is to use the bifurcation point of the medial axis. To this end, it is necessary to obtain the skeleton of the 3-D model. A complete description of the skeletonization algorithm can be found in [41]. This algorithm utilizes an average outward flux measure to distinguish skeletal points from nonskeletal ones and combines this measure with a topology preserving thinning procedure. The approach is fully automatic and requires no user interaction. It is virtually parameter free and has low computational complexity.

Fig. 4 shows the medial curves for several cases from our database obtained by using this skeletonization algorithm.

E. Morphological Characterization Pipeline

In this section, a complete and efficient image-based methodology for the morphological analysis of cerebral aneurysms on a patient-specific basis is presented. Although the individual components of the modeling pipeline may not be entirely original, this methodology allows for the first time the modeling of a large number of aneurysms in a timely manner. The key component of this pipeline is the set of new shape descriptors proposed, which capture the full 3-D geometry of the aneurysms.

The characterization pipeline is summarized in Fig. 5. Starting with the medical image acquisition, segmentation is performed in order to obtain the numerical models. Then, the skeleton is extracted for isolating and normalizing such models. Finally, global shape invariants are calculated.

IV. RESULTS

Two experiments were conducted to assess the influence of different processing steps in the computation of the aneurysmal moment-based shape descriptors. In particular, the factors studied include the use of different segmentation methods for obtaining the aneurysmal geometry (i.e., deformable model versus implicit deformable surface), and the influence of the selection of different cut planes for isolating aneurysms while preserving information about the adjacent vessels.
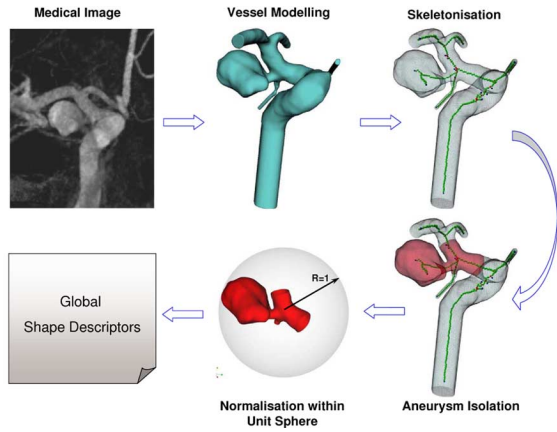
Fig. 5. Illustration of the processing steps necessary for defining the shape invariants.

TABLE III
FROM A COLLECTION OF 22 ANEURYSMS, EACH WITH TWO DIFFERENT MODELS (FROM TWO SEGMENTATION METHODS), NUMBER OF ANEURYSMS WHOSE SECOND MODEL IS RANKED, AMONG ALL THE MODELS, IN THE FIRST POSITIONS OF PROXIMITY TO THEIR FIRST MODEL. NEAREST-NEIGHBOR CLASSIFIER WITH EUCLIDIAN METRIC IS USED IN BOTH THE SPACE OF GMI AND THE SPACE OF ZMI

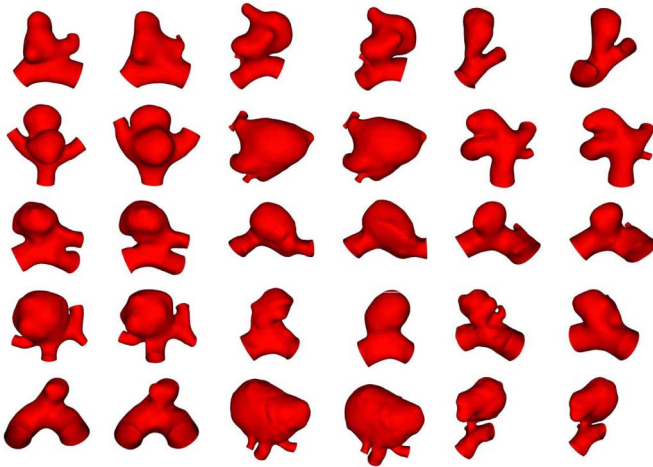| Order	GMI				ZMI			
	Surface		Volume		Surface		Volume	
	CM	BP	CM	BP	CM	BP	CM	BP
1	55% (12)	36% (8)	50% (11)	27% (6)	91% (20)	77% (17)	82% (18)	77% (17)
2	9% (2)	14% (3)	14% (3)	9% (2)	5% (1)	14% (3)	14% (3)	9% (2)
3	0% (0)	5% (1)	9% (2)	27% (6)	0% (0)	0% (0)	0% (0)	5% (1)

Fig. 6. Three-dimensional aneurysm models obtained by using two different segmentation models, left: based on deformable surface models and right: based on region based implicit deformable surfaces. See Section III.

Finally, the value of the proposed shape indices as reliable rupture risk descriptors is assessed on a database of 55 aneurysms.

A. Segmentation Methods

To assess the influence of the segmentation method on the calculation of the moment invariants, a study over a population of 22 aneurysm models, segmented with two alternative methods, has been performed. As already mentioned in Section III, the first segmentation method is based on deformable models [35], [36], whereas the second method considers region-based implicit deformable surfaces [37]. Fig. 6 shows some examples of 3-D isolated aneurysm models obtained by using each of these methods.

It should be noted that the purpose of this experiment is not to compare the performance of the segmentation methods, but rather to establish the robustness of the shape descriptors when different segmentation methods are considered. These methods have been properly and independently optimized exclusively from the segmentation performance point of view, as given in [35] and [37]. However, it is beyond the scope of this paper to

explore such segmentation procedures and develop any further improvements to them.

It is worth noting that the GMI provide 12 shape features for each isolated model, whereas the ZMI provide 121 when moments up to order 20 are used [21]. Only 20 orders have been used because this represents a good compromise between computational time and accuracy in the shape description (see Fig. 1).

The isolated models obtained from each segmentation method were aligned, and a nearest-neighbor classifier was used. In these experiments, the Euclidean distance has been used as the metric for the classifier. A ranked list of neighbors was obtained for each model. The results of the segmentation experiments, for both the GMI and the ZMI, are summarized in Table III. The column labeled as *order* describes the ranking as nearest-neighbor that the same model segmented with the other method obtains.

It is worth noting that in those cases where the first ranked model was not the same model, the segmentation method did, in fact, provide substantially different results. This was especially critical around the aneurysmal neck where subtle variations are thought to play a significant role in the progression and eventual rupture of the aneurysms. Hence, the sensitivity of the shape descriptors to shape variations in this region is indeed a desirable property, although this leads to the problem of improving the segmentation methods or the image resolution, which is out of the scope of this paper.

It is clear from the results that ZMI perform better than GMI descriptors. This can be easily interpreted since GMI are only able to capture lower spatial frequencies up to order 3. In addition, surface-based moments consistently show better results than volume-based moments. Analogously, the cases where the bifurcation point has been used to achieve translational invariance show consistently poorer results than the cases using the center of mass. Although *a priori*, the bifurcation points might seem more robust, especially when different cut planes are selected, our results indicate that this may not always be the case. In particular, the sensitivity of the skeletons to the variations in the segmented models seem larger from these results. Therefore, although not completely conclusive by themselves, these results suggest that surface-based ZMI centered by the center of
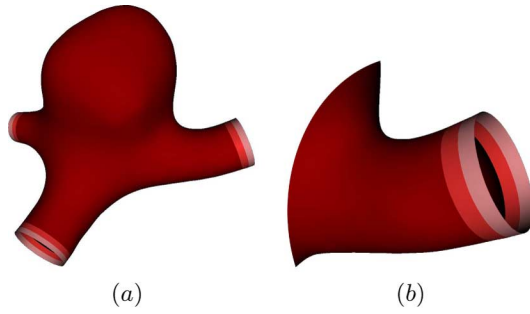
Fig. 7. (a) Example illustrating the different cut planes used to assess the sensitivity of the invariants to errors in the cut-plane selection, and (b) detail of the selected cut-planes in image (a). For this particular case (terminal aneurysm with three adjacent vessels), 27 different aneurysm models were obtained.

mass are the most robust against the use of different segmentation methods.

B. Sensitivity to Cut-Planes Definition

In this section, the sensitivity to cut-plane selection during aneurysm isolation has been investigated in three aneurysms. An example of each of the lateral, terminal, and bifurcation aneurysms has been selected for such purpose.

For each case, three different cut-planes at each one of the adjacent vessels were performed. This led to different aneurysm models with their corresponding adjacent vessels. The selection of the different cut-planes is illustrated in Fig. 7 and provides $3 \times 3 = 9$ models for the lateral case, and $3 \times 3 \times 3 = 27$ models for the both bifurcation and terminal types.

In order to assess the robustness of the moment invariants, two different analyses were performed. The first one is related to the dispersion from a mean model as consequence of the cut-plane selection. In the second one, the variability related to cut-plane definition is related to the classification performance.

1) Dispersion: The results of this experiment have been analyzed by using the relative error between the shape indices from the perturbed aneurysm models and the mean model for each aneurysm type. The relative error has been chosen in order to normalize the GMI and ZMI values, and therefore to enable their comparison. Then, for each aneurysm type the relative error of the ith component for the jth perturbed model $(\epsilon_{i,j})$ is computed as

$$\epsilon_{i,j} = \frac{x_{i,j} - \bar{x}_i}{\bar{x}_i} \qquad (15)$$

where $\bar{x}_i$ is the ith mean component of the feature vector obtained from averaging over all models, and $x_{i,j}$ is the ith shape index derived from the jth perturbed aneurysm model; $i = 1, \ldots, D$ and $j = 1, \ldots, n$, where D is the feature space dimension and n is the number of perturbed models for each aneurysm type.

A principal component analysis (PCA) has been performed to reduce the dimensionality of the data. It has been found that a few components, typically between 3 and 5, accounted for 99% of the variance in the original feature space. Such dimensionality reduction has been applied to all moment invariant types.

TABLE IV
STANDARD ERROR OF THE MEAN (SEM) OF THE RELATIVE ERROR BETWEEN THE SHAPE INDICES, GMI (LEFT) AND ZMI (RIGHT) FROM THE PERTURBED MODELS AND THE AVERAGE MODEL. CASES IN WHICH GMI PERFORMS BETTER THAN ZMI ARE HIGHLIGHTED IN BOLD

Type	Moment Invariant	Mean	Median	Min	Max
L	Surface$_{CM}$	1.50 / 0.18	1.50 / 0.19	0.63 / 0.05	2.37 / 0.34
	Surface$_{BP}$	0.28 / 0.23	0.28 / 0.18	0.25 / 0.10	**0.30** / 0.47
	Volume$_{CM}$	3.80 / 0.17	3.80 / 0.16	3.80 / 0.06	3.80 / 0.32
	Volume$_{BP}$	**0.16** / 0.21	**0.16** / 0.22	**0.03** / 0.09	**0.29** / 0.32
B	Surface$_{CM}$	0.44 / 0.11	0.44 / 0.07	0.44 / 0.03	0.44 / 0.26
	Surface$_{BP}$	0.06 / 0.08	0.06 / 0.03	0.06 / 0.04	**0.06** / 0.27
	Volume$_{CM}$	**0.06** / 0.09	0.06 / 0.05	**0.02** / 0.03	**0.11** / 0.27
	Volume$_{BP}$	0.06 / 0.03	0.06 / 0.03	0.06 / 0.01	0.06 / 0.05
T	Surface$_{CM}$	0.25 / 0.10	0.25 / 0.09	0.08 / 0.03	0.43 / 0.19
	Surface$_{BP}$	4.30 / 0.10	4.30 / 0.07	1.58 / 0.03	7.01 / 0.22
	Volume$_{CM}$	1.11 / 0.10	1.11 / 0.08	1.11 / 0.03	1.11 / 0.22
	Volume$_{BP}$	0.61 / 0.11	0.61 / 0.08	0.21 / 0.03	1.00 / 0.25

The standard error of the mean (SEM) of each component has been considered to quantify the dispersion in each aneurysm type. Such value has been averaged over all the perturbed models for each component. Then, the different components have also been averaged to provide a single measure indicating the variability for a particular type of moments. The results for the relative error derived from the three models are presented in the Table IV. Several statistical parameters have been used in order to better characterize the distribution of errors. As can be seen, ZMI perform better in a large majority of the cases. Only in a few cases, highlighted in bold, GMI would provide better results. However, the effect of the centering methods in the computation does not show significant differences in the SEM results.

2) Classification: In this second analysis, we are interested in evaluating the classification performance related to the variability in cut-plane selection. The classification problem in this case answers the question: for each of the aneurysms in the dataset, is there any other aneurysm that is closer than any of the models of the same aneurysm?

In order to answer this question, a nearest neighbor classifier has been used. On the contrary that in the experiment for the segmentation method sensitivity, in this case we have at least nine perturbed models for each aneurysm. Thus it has been feasible the use of the Mahalanobis distance as similarity measurement.

The population covariance matrix has been estimated from the pooled sample covariance matrix, which in the case of g groups or classes, π_i, is defined as

$$\mathbf{S}_p = \frac{1}{N - g} \sum_{i=1}^{g} (N_i - 1) \mathbf{S}_i \qquad (16)$$

where $N = N_1 + N_2 + \cdots + N_g$ are the samples sizes for each group π_i, and $\mathbf{S}_i$ is the sample group covariance matrix. In our case $\pi = \{\pi_{\text{Lateral}}, \pi_{\text{Bifurcation}}, \pi_{\text{Terminal}}\}$.

The calculus of the Mahalanobis distance for each aneurysm type is as follows. To avoid singular covariance matrices, PCA has been applied to reduce the dimensionality of the feature

TABLE V
FOR EACH OF THE THREE PERTURBED MODELS, NUMBER OF THE OTHER
ANEURYSMS, FROM THE DATA-SET OF 55, WRONGLY CLASSIFIED AS CLOSER
TO THIS MODEL THAN ITS OWN PERTURBED MODELS. MAHALANOBIS
DISTANCE IS USED AS THE METRIC OF A NEAREST NEIGHBOR CLASSIFIER IN A
SPACE OF REDUCED DIMENSIONALITY

| Type	GMI				ZMI			
	Surface		Volume		Surface		Volume	
	CM	BP	CM	BP	CM	BP	CM	BP
L	65% (35)	52% (28)	35% (19)	17% (9)	0% (0)	0% (0)	0% (0)	0% (0)
B	56% (30)	22% (12)	6% (3)	22% (12)	0% (0)	0% (0)	2% (1)	0% (0)
T	0% (0)	78% (42)	76% (41)	69% (37)	0% (0)	4% (2)	0% (0)	0% (0)

Fig. 8. Classification rate obtained by LDA, MDA, and QDA displayed as a function of the number of features selected by SFS on the surviving principal components for the four types of ZMI.

space. The number of components kept was such that they accounted for 99% of the variance in the original dataset. Then, the pooled covariance matrix and the complete data-set were projected onto the reduced feature space. In this projected space, the Mahalanobis distance between the origin (average model) and both, the perturbed models of the same aneurysm and the other aneurysms, were computed. Table V shows the number of wrongly classified cases, that is, the cases that belonging to the data-set are closer to the average model than any of the perturbed models. It is clear from these results that GMI are not sufficiently robust to account for these variations, whereas ZMI are robust. Both centering methods, CM and BP present similar performances.

C. Rupture Risk Prediction

As has been evidenced in the previous subsections that ZMI are more robust than GMI. In order to asses the value of such invariants as features which, by encapsulating morphological information, may predict the risk of rupture, three types of discriminant analysis (DA)—linear discriminant analysis (LDA), Mahalanobis discriminant analysis (MDA), and quadratic discriminant analysis (QDA)—were performed. To this end, the 55 avalaible aneurysms were divided in two groups, namely, those presenting SAH (*ruptured*) and those without SAH (*unruptured*).

It is a well-established fact, that all of the commonly used classifiers can suffer from the "curse of dimensionality." However, an exact relationship between the probability of misclassification, the number of training samples, the number of features, and the true parameters of the class-conditional densities is very difficult to establish. As a general guideline, Jain and Chandrasekaran [42] have suggested that the training samples per class n should be at least five to ten times the dimension of the feature space D. In our small sample (total 55 training patterns), the optimal number of features is about 11 which equals $n/5$ ($n = 55$), where n is the number of training patterns. The rule-of-thumb of having less than 10 features is on the safe side in our case.

In order to reduce the dimensionality of the feature space, PCA was performed keeping 99% of the population variance.
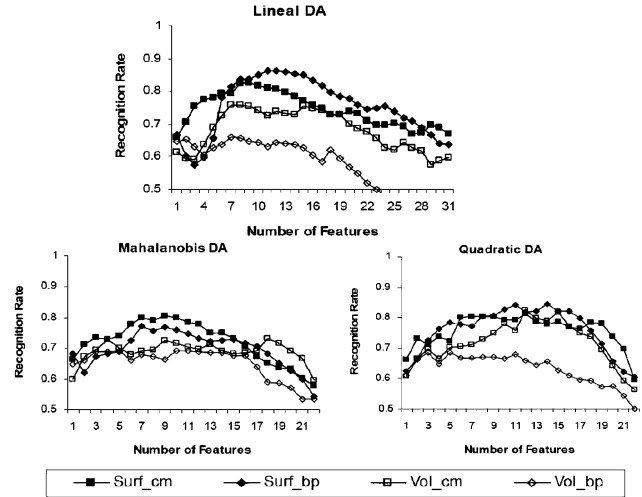
On the retained features, a sequential forward selection (SFS) was subsequently applied.

For estimating the recognition rate of the considered classification scheme, cross-validation was used. Given the reduced size of our database, a variation of stratified leave-one-out cross validation has been used. Concretely, we consider all the training sets formed by removing two samples from the dataset, one from each of the two classes (ruptured and unruptured). This gives a total of $31 \times 24 = 744$ different splittings. The estimator of the recognition rate is the average of the results obtained over all the so constructed evaluation sets. This estimator is unbiased, under the assumption that the classification scheme is not too sensitive to removing two samples from the training set [43], and an estimation of its standard deviation is given by the formula $\sigma = \sqrt{r(1-r)/n}$, where r is the estimated recognition rate and n is the cardinality of the dataset. This non-sensitivity hypothesis becomes less realistic when considering more features. This is the essential reason behind the rule-of-thumb of Jain and Chandrasekaran [42].

The rupture risk prediction has been estimated from different number of features, selected by SFS (after PCA), from the four types of ZMI considered: either from the volume or the surface, and centred either with the CM or the BP. The results are displayed in Fig. 8. For the safe range until 10 features, we obtain a better estimated recognition rate for the surface based ZMI of around $80\% \pm 5\%$, with slightly better performance of the ones centered with the CM. The similarity of the results obtained from the two types of surface based ZMI does not allow us to assert the superiority of either of them. But, on the other side, this similarity gives an independent argument for the reliability of the result.

These results have been contrasted with the rupture risk prediction obtained from the usual aneurysm size and aspect ratio (AR), and their combination, estimated on the same dataset by using the same cross-validation method. These recognition rates are summarized in Table VI. The best performance result was

TABLE VI
SIZE AND ASPECT RATIO AS RUPTURE PREDICTORS, SEVERAL DISCRIMINANT
ANALYSIS ARE PERFORMED

Discriminant Analysis	Size	Aspect Ratio	Size Aspect Ratio
Linear	51.6%	**65.7%**	53.7%
Mahalanobis	54.0%	53.3%	62.4%
Quadratic	61.9%	54.2%	55.4%

lower than 66%, clearly inferior than the recognition rates obtained from ZMI.

It is also worth mentioning that only 59% of the 31 ruptured aneurysm had $AR \geq 1.6$ (the cutoff previously reported by Ujiie *et al.* [14]), whereas 79% of the 24 unruptured had an $AR < 1.6$, which clearly illustrates the ongoing controversy [17]–[19]. The positiveness of the AR values suggests that the data may follow rather a log-normal than a normal distribution. The two samples, as well as the union of them, are compatible with a log-normal distribution with 95% confidence level for the Lilliefors, Shapiro–Wilks and χ^2 tests. An ANOVA test was subsequently performed on the logarithm of the AR values. No significant differences at 95% confidence level were found between the population of ruptured and unruptured aneurysms, neither in variance nor in mean, indicating that any actual difference between both populations must be small.

V. CONCLUSION AND DISCUSSION

The importance of the introduction of morphological features in the clinical evaluation of intracranial aneurysms is underlined by the results of hemodynamic studies demonstrating complex relationships between shape irregularities and hemodynamic stresses on the aneurysmal wall. These contribute to inflammatory processes, thrombus formation and, eventually, to rupture [4]. To this end, better shape representations should be designed encapsulating the criteria that neuroradiologists follow to make clinical decisions. In this work, moment invariants are used with such aim. Moment invariants are defined by considering the full 3-D geometry of the aneurysms in contrast to previous approaches.

In particular, the correlation between rupture risk and geometrical shape parameters has been investigated by using two different moment-based descriptors: GMI and ZMI. These shape indices are obtained from linear combinations of geometric moments, which are calculated over non-structured triangular meshes, thus allowing subvoxel precision. Unfortunately, GMI are difficult to derive, and only a small number of them are explicitly derived up to order 3 [23], [29]. This implies that only low frequency details are encapsulated in such descriptors. To overcome these limitations, Zernike moments have been used.

For both, GMI and ZMI, four different calculation approaches have been followed: $Surface_{CM}$, $Surface_{BP}$, $Volume_{CM}$, and $Volume_{BP}$, which differ in the centering point (BP versus CM) and whether the complete volume or just its outer surface has been used for their calculation. Promising results, $80\% \pm 5\%$ correct classification rates, have been obtained in a reasonable sized database containing 55 aneurysms. In contrast, when the classical aspect ratio index is used, at most a $66\% \pm 7\%$ of correct classification is reached.

It is worth noting that, in this work, the adjacent vessels of the aneurysmal sac have been considered in the computation of the shape descriptors. This is in contrast to previous research works [4], [16] which only take into account the aneurysmal sac. With the inclusion of a portion of the parent vessels, some predictive value to the characterization of the aneurysms is added since flow-related information is implicitly incorporated. Even though new challenges are faced as a consequence of the need to define the cut-planes, previous approaches needed also to tackle the problem of how to isolate the aneurysmal sac by selecting the neck cut-plane, which is usually even more ill-defined.

The robustness of these descriptors has been assessed in two different scenarios, namely, robustness to segmentation differences and robustness to cut plane selection. In both cases, the performance of ZMI was superior to that of GMI. Thus, it is concluded that ZMI show richer description properties and are more robust to small perturbations of the models. In particular, surface-based ZMI centered to the CM consistently provide good results. This is expected since the Zernike moments constitute a complete basis that eventually enables the reconstruction of the original model. However, to reach accurate reconstructions, it is necessary to consider high orders leading to high-dimensional feature spaces with their associated problems.

No conclusive results were obtained as to whether the CM or the BP should be used for centering the models. Although the CM performed better in some cases, this finding was not always consistent. In fact, the normalization for translation invariance may be closely coupled to the scaling, and therefore, further research is necessary on this issue. The method proposed by Novotni and Klein [33], based on fixing the spread of the object, has been used in this study to obtain scale invariance. Future work will be devoted to obtain a suitable value for such spread that optimizes the results. Further investigation is also required to assess the influence of other errors in the model definition. This may include the accuracy with which the nearby vessels are modeled as a consequence of scanner's resolution, the segmentation algorithm, or postprocessing steps like smoothing. Such issues need to be assessed by using phantoms to evaluate the effect of the artefacts on the shape descriptors.

It should also be noted that an unproven assumption of this study, and of all the other previous works on characterization of aneurysms [4], [16], [17], is that aneurysms do not change dramatically their size and shape when they rupture. Although a decrease in size with rupture has been tentatively postulated [44], [45], no studies have definitively documented this phenomenon. On the other hand, several neurosurgical experts raised the opinion, that rupture does not cause major changes in the size and shape of an aneurysm [12], [46], [47]. However, since the configuration of aneurysms might change following its rupture, there is a need to conduct prospective studies for analyzing this possibility. This will be essential in assessing if quantitative shape analysis can determine the risk of rupture.

In summary, we have reported and analyzed two moment-based methods to characterize the three dimensional morphology of aneurysms. The possibility that ZMI can predict rupture risk is exciting, although, despite the encouraging

results obtained, more cases must be studied for establishing the clinical value of this technique.

APPENDIX I
GEOMETRIC MOMENTS COMPUTATION BY USING THE DIVERGENCE THEOREM

The Divergence Theorem: The Divergence Theorem for continuous functions is known as Gauss's theorem in 3-D and relates a surface integral over a closed surface in 3-D to a integral over the enclosed volume. The Gauss's theorem can be stated as follows:

$$\int_{\Omega} \nabla \cdot \mathbf{F} \, d\mathbf{x} = \int_{\Gamma} \mathbf{F} \cdot \hat{\mathbf{n}} \, d\sigma \qquad (17)$$

where Ω is the volume domain and Γ its boundary. $\mathbf{F} = (F_1, F_2, F_3)^T$, $F_i = F_i(\mathbf{x})$ is a differentiable vectorial field, $\hat{\mathbf{n}} = (n_x, n_y, n_z)^T$ is the outward normal vector to the surface, and $d\sigma$ is the infinitesimal surface element.

Volume-based geometric moments are defined by (2), where the density function is a binary partition function

$$f(\mathbf{x}) = \begin{cases} 1, & \text{if } \mathbf{x} \in \Omega, \\ 0, & \text{otherwise.} \end{cases}$$

Thus, the integral to be performed is

$$m_{\mathrm{pqr}} = \int_{\Omega} x^p y^q z^r \, d\mathbf{x}$$

Hence, we can look for a vectorial field $\mathbf{F}$ satisfying $\nabla \cdot \mathbf{F} \equiv x^p y^q z^r$. The solution is easily obtained and, although it is not unique, the most symmetrical case can be chosen. Thus, applying the divergence theorem for this solution, the volume-based geometric moments can be written as

$$m_{\mathrm{pqr}} = \int_{\Gamma} \frac{x^p y^q z^r}{3} \left(\frac{x}{p+1}, \frac{y}{q+1}, \frac{z}{r+1} \right) \cdot \hat{\mathbf{n}}(\mathbf{x}) \, d\sigma. \qquad (18)$$

In the discrete case, the divergence theorem relates a sum of a function over a discrete and closed surface to a sum of the function over the enclosed region. The object surface in such a discrete case is formed by a disjoint union of planar 3-D polygons, $\Gamma = \bigcup_{j=1}^{N} \Gamma_j$, and (18) becomes

$$m_{\mathrm{pqr}} = \sum_{j=1}^{N} \int_{\Gamma_j} \frac{x^p y^q z^r}{3} \left(\frac{x n_{xj}}{p+1} + \frac{y n_{yj}}{q+1} + \frac{z n_{zj}}{r+1} \right) d\sigma. \qquad (19)$$

Accordingly, (19) can be rewritten as a sum over all the polygons Γ_j forming the object surface, $m_{\mathrm{pqr}} = \sum_j m_{\mathrm{pqr}}^j$. In the case of triangular meshes, the integral m_{pqr}^j in each triangular element can be analytically computed. A detailed description of this is presented in the next subsection.

Geometric Moments Computation Over Each Triangle: Assuming that each discrete polygonal surface, Γ_j, is defined by a triangle, with vertices $\mathbf{P}_{j,i}$ for $1 \leq i \leq 3$, the unitary outer normal $\hat{\mathbf{n}}_j$ to each triangle can be calculated as: $\hat{\mathbf{n}}_j = (\mathbf{P}_{j,21})/(\|\mathbf{P}_{j,21}\|) \times (\mathbf{P}_{j,31})/(\|\mathbf{P}_{j,31}\|)$, where $\mathbf{P}_{j,21} = \mathbf{P}_{j,2} - \mathbf{P}_{j,1}$, and $\mathbf{P}_{j,31} = \mathbf{P}_{j,3} - \mathbf{P}_{j,1}$. The plane equation that describes each surface facet in the space is

$$\mathbf{P}_{j,\mathbf{x}1}^T \cdot \hat{\mathbf{n}}_j = 0 \qquad (20)$$

where $\mathbf{P}_{j,\mathbf{x}1} = \mathbf{P}_{j,\mathbf{x}} - \mathbf{P}_{j,1} = (x - x_1, y - y_1, z - z_1)^T$, and $\hat{\mathbf{n}}_j = (n_{jx}, n_{jy}, n_{jz})^T$. For the sake of clarity, in some manipulations, j-subindices will be omitted, although all expressions will refer to the Γ_j surface patch.

In order to compute the integral m_{pqr}^j, it is necessary to express the points of the triangle Γ_j immersed in the space in terms of some 2-D coordinates on the triangular surface. To this end, *natural coordinates* of the surface Γ_j are good candidates. Natural coordinates are dimensionless and are defined with respect to the length, area, or volume of the element, rather than with respect to the global 3-D coordinate system. In our case, the natural coordinates for a triangle Γ_j are the *triangular coordinates*. Any point in the triangular surface $\mathbf{P} \in \Gamma_j$ defines three lines connecting it to each of the vertices, which divides the triangle Γ_j into three areas A_1, A_2, and A_3. The area coordinates are defined as the proportions of these areas

$$\ell_1 = \frac{A_1}{A}, \quad \ell_2 = \frac{A_2}{A}, \quad \ell_3 = \frac{A_3}{A} \qquad (21)$$

where A is the area of the triangle Γ_j. Obviously, they satisfy the constraint $\ell_1 + \ell_2 + \ell_3 = 1$. Thus, only two of them are needed to coordinate the triangular surface, but keeping the three of them in a symmetrical way has some advantages to compute the integrals.

These triangular coordinates are indeed a linear transformation from the 3-D Cartesian coordinates. Hence, there exists a matrix $\mathbf{A}$ defining the transformation $\{\ell_1, \ell_2, \ell_3\} \rightarrow \{x, y, z\}$ as

$$\mathbf{x} = \mathbf{A}\boldsymbol{\ell} \qquad (22)$$

where $\mathbf{x} = (x, y, z)^T$ and $\boldsymbol{\ell} = (\ell_1, \ell_2, \ell_3)^T$. By denoting conveniently the components of the matrix $\mathbf{A}$, this can be equivalently expressed as

$$x = \sum_{i=1}^{3} x_i \ell_i, \quad y = \sum_{i=1}^{3} y_i \ell_i, \quad z = \sum_{i=1}^{3} z_i \ell_i.$$

When expressed in triangular coordinates, the integral m_{pqr}^j becomes a linear combination of terms of the form $\int_A \ell_1^k \ell_2^l \ell_3^m \, d\sigma$, with k, l, and m nonnegative integers. These integrals can be computed by expressing the differential area in triangular coordinates [48]

$$d\sigma = 2A \, d\ell_1 d\ell_2.$$

The result of the integral is then

$$\int_A \ell_1^k \ell_2^l \ell_3^m \, d\sigma = 2A \frac{k!l!m!}{(k+l+m+2)!}. \tag{23}$$

Finally, recombining these terms, the integral m_{pqr}^j can be expressed as

$$m_{p_1 p_2 p_3}^j = \frac{2A}{3(|\mathbf{p}|+3)!} \sum_{\mathbf{k}=0}^{\mathbf{P}} \binom{\mathbf{p}}{\mathbf{k}} x_3^{p_1-k_1} y_3^{p_2-k_2} z_3^{p_3-k_3} (|\mathbf{p}|-|\mathbf{k}|)!$$
$$\times \sum_{\mathbf{j}=0}^{\mathbf{k}} \binom{\mathbf{k}}{\mathbf{j}} x_1^{j_1} y_1^{j_2} z_1^{j_3} x_2^{k_1-j_1} y_2^{k_2-j_2} z_2^{k_3-j_3} |\mathbf{j}|!(|\mathbf{k}|-|\mathbf{j}|)!$$
$$\times (\chi_1 + \chi_2 + \chi_3 + (\chi_1 - \chi_2)|\mathbf{j}| + (\chi_2 - \chi_3)|\mathbf{k}| + \chi_3|\mathbf{p}|)$$

where the following notation has been used:

$$\sum_{\mathbf{k}=0}^{\mathbf{P}} = \sum_{k_1=0}^{p_1} \sum_{k_2=0}^{p_2} \sum_{k_3=0}^{p_3}, \quad \binom{\mathbf{p}}{\mathbf{k}} = \prod_{i=1}^{3} \binom{p_i}{k_i}$$

$$\chi_i = \frac{x_i n_x}{p_1+1} + \frac{y_i n_y}{p_2+1} + \frac{z_i n_z}{p_3+1}, \quad |\mathbf{p}| = \sum_{i=1}^{3} p_i.$$

Newton's binomial $(a+b)^n = \sum_{k=0}^{n} \binom{n}{k} a^k b^{n-k}$ has been used to expand expressions of the form $(\xi_1 \ell_1 + \xi_2 \ell_2 + \xi_3 \ell_3)^{p_i}$, where $i = 1, 2, 3$ and $\xi = x, y, z$.

ACKNOWLEDGMENT

REFERENCES

[1] B. Weir, "Unruptured intracranial aneurysms: A review," *J. Neurosurg.*, vol. 96, pp. 3–42, 2002.

[2] S. Juvela, M. Porras, and K. Poussa, "Natural history of unruptured intracranial aneurysms: Probability of and risk factors for aneurysm rupture," *J. Neurosurg.*, vol. 93, pp. 379–387, Sep. 2000.

[3] R. D. Ecker and L. N. Hopkins, "Natural history of unruptured intracranial aneurysms," *Neurosurg. Focus*, vol. 17, no. 5, pp. 1–5, Nov. 2004.

[4] S. Rohde, K. Lahmann, J. Beck, R. Nafe, B. Yan, A. Raabe, and J. Berke-feld, "Fourier analysis of intracranial aneurysms: Towards an objective and quantitative evaluation of the shape of aneurysms," *Neuroradiology*, vol. 47, pp. 121–126, 2005.

[5] S. Juvela, "Prehemorrhage risk factors for fatal intracranial aneurysm rupture," *Stroke*, vol. 34, pp. 1852–1858, 2003.

[6] W. Schievink, "Intracranial aneurysms," *New Eng. J. Med.*, vol. 336, pp. 28–41, Jan. 1997.

[7] D. Woo and J. Broderick, "Genetics of intracranial aneurysm," *J. Stroke Cerebrovascular Diseases*, vol. 11, no. 5, pp. 230–240, 2002.

[8] D. O. Wiebers *et al.*, "Unruptured intracranial aneurysms-risk of rupture and risks of surgical intervention," *New Eng. J. Med.*, vol. 339, pp. 1725–1733, 1998.

[9] D. O. Wiebers *et al.*, "Unruptured intracranial aneurysms: Natural history, clinical outcome, and risks of surgical and endovascular treatment," *Lancet*, vol. 362, pp. 103–110, Jul. 2003.

[10] K. Kayembe, M. Sasahara, and F. Hazama, "Cerebral aneurysms and variations in the circle of willis," *Stroke*, vol. 15, pp. 846–850, 1984.

[11] T. M. Liou and S. N. Liou, "A review of in vitro studies of hemodynamic characteristics in terminal an lateral aneurysm models," in *Proc. Nat. Sci. Council ROC(B)*, 1999, vol. 23, no. 4, pp. 133–148.

[12] T. R. Forget, R. Benitez, E. Veznedaroglu, A. Sharan, W. Mitchell, M. Silva, and R. H. Rosenwasser, "A review of size and location of ruptured intracranial aneurysms," *Neurosurgery*, vol. 49, no. 6, pp. 1322–1326, Dec. 2001.

[13] S. Juvela, M. Porras, and O. Heiskanen, "Natural history of unruptured intracranial aneurysms: A long-term follow-up study," *J. Neurosurg.*, vol. 79, no. 2, pp. 174–182, Aug. 1993.

[14] H. Ujiie, H. Tachibana, O. Hiramatsu, A. L. Hazel, T. Matsumoto, Y. Ogasawara, H. Nakajima, T. Hori, K. Takakura, and F. Kajiya, "Effects of size and shape (aspect ratio) on the hemodynamics of saccular aneurysms: A possible index for surgical treatment of intracranial aneurysms," *Neurosurgery*, vol. 45, no. 1, pp. 119–130, Jul. 1999.

[15] B. Ma, R. E. Harbaugh, and M. L. Raghavan, "Three-dimensional geometrical characterization of cerebral aneurysms," *Ann. Biomed. Eng.*, vol. 32, no. 2, pp. 264–273, Feb. 2004.

[16] M. L. Raghavan, B. Ma, and R. E. Harbaugh, "Quantified aneurysm shape and aneurysm rupture," *J. Neurosurg.*, vol. 102, pp. 355–362, 2005.

[17] H. Ujiie, H. Tamano, K. Sasaki, and T. Hori, "Is the aspect ratio a reliable index for predicting the rupture of saccular aneurysms?," *Neurosurgery*, vol. 48, no. 3, pp. 495–503, 2001.

[18] B. Weir, C. Amidei, G. Kongable, J. M. Findlay, N. F. Kassell, J. Kelly, L. Dai, and T. G. Karrison, "The aspect ratio (dome/neck) of ruptured and unruptured aneurysms," *J. Neurosurg.*, vol. 99, pp. 447–451, 2003.

[19] A. Nader-Sepahi *et al.*, "Is aspect ratio a reliable predictor of intracranial aneurysm rupture?," *Neurosurgery*, vol. 54, pp. 1343–1348, 2004.

[20] J.-F. Mangin, F. Poupon, E. Duchesnay, D. Rivière, A. Cachia, D. L. Collins, A. C. Evans, and J. Régis, "Brain morphometry using 3-D moment invariants," *Med. Image Anal.*, vol. 8, pp. 187–196, 2004.

[21] M. Novotni and R. Klein, "Shape retrieval using 3-D Zernike descriptors," *Comput.-Aided Des.*, vol. 36, pp. 1047–1062, Jan. 2004.

[22] J. Flusser, J. Boldys, and B. Zitová, "Moment forms invariant to rotation and blur in arbitrary number of dimensions," *IEEE Trans. Pattern Anal. Mach. Intell.*, vol. 25, no. 2, pp. 234–246, Feb. 2003.

[23] C.-H. Lo and H.-S. Don, "3-D moments forms: Their construction and application to object identification and positioning," *IEEE Trans. Pattern Anal. Mach. Intell.*, vol. 11, no. 10, pp. 1053–1064, Oct. 1989.

[24] L. Yang, F. Albregtsen, and T. Taxt, "Fast computation of 3-D geometric moments using a discrete divergence theorem and a generalization to higher dimensions," *Graph. Models Image Process.*, vol. 59, no. 2, pp. 97–108, Mar. 1997.

[25] A. G. Mamistvalov, "n-dimensional moment invariants and conceptual mathematical theory of recognition n-dimensional solids," *IEEE Trans. Pattern Anal. Mach. Intell.*, vol. 20, no. 8, pp. 819–831, Aug. 1998.

[26] M. Zribi, "Description of three-dimensional gray-level objects by the harmonic analysis approach," *Pattern Kecogn. Lett.*, vol. 23, no. 1–3, pp. 235–243, Dec. 2002.

[27] A. R. Edmonds, *Angular Momentum in Quantum Mechanics*. Princeton, NJ: Princeton Univ. Press, 1996.

[28] F. Poupon, "Parcellisation systematique du cerveau en volumes d'mteret. le cas des structures profondes," Ph.D. dissertation, INSA, Lyon, France, Dec. 1999.

[29] G. Burel and H. Hénocq, "Three-dimensional invariants and their application to object recognition," *Signal Process.*, vol. 45, pp. 1–22, 1995.

[30] C.-H. Teh and R. T. Chin, "On image analysis by the methods of moments," *IEEE Trans. Pattern Anal. Mach. Intell.*, vol. 10, no. 4, pp. 496–513, Jul. 1988.

[31] A. Khotanzad and Y. H. Hong, "Invariant image recognition by Zernike moments," *IEEE Trans. Pattern Anal. Mach. Intell.*, vol. 12, no. 5, pp. 489–497, May 1990.

[32] N. Canterakis, "3-D Zernike moments and Zernike affine invariants for 3-D image analysis and recognition," presented at the 11th Scand. Conf. Image Anal., Kangerlussuaq, Greenland, Jun. 1999 [Online]. Available: citeseer.ist.psu.edu/504643.html

[33] M. Novotni, G.-J. Park, R. Wessel, and R. Klein, "Evaluation of kernel based methods for relevance feedback in 3-D shape retrieval," presented at the 4th Int. Workshop Content-Based Multimedia Indexing (CBMI'05), Riga, Latvia, Jun. 2005.

[34] T. F. Massound, G. Guglielmi, F. Vinuela, and G. R. Duckwiller, "Experimental saccular aneurysms I. Review of surgycally-constructed models and their laboratory applications," *Neuroradiology*, vol. 36, pp. 537–546, 1994.

[35] J. R. Cebral, M. Hernandez, A. F. Frangi, C. M. Putman, R. Pergolizzi, and J. E. Burgess, "Subject-specific modeling of intracranial aneurysms," presented at the SPIE Med. Imag. Conf., San Diego, CA, Feb. 14–19, 2004.

[36] P. J. Yim, G. B. C. Vasbinder, V. B. Ho, and P. L. Choyke, "Iso-surfaces as deformable models for magnetic resonance angiography," *IEEE Trans. Med. Imag.*, vol. 22, no. 7, pp. 875–881, Jul. 2003.

[37] M. Hernandez and A. F. Frangi, "Non-parametric geodesic active regions: Method and evaluation for cerebral aneurysms segmentation in 3DRA and CTA," *Med. Image Anal.*, vol. 11, pp. 224–241, 2006.

[38] G. Taubin, "A signal processing approach to fair surface design," *Comput. Graphics Proc.*, pp. 351–358, 1995.

[39] J. R. Cebral and R. Lohner, "From medical images to anatomically accurate finite element grids," *Int. J. Num. Meth. Eng.*, vol. 51, pp. 985–1008, 2001.

[40] J. R. Cebral, M. A. Castro, S. Appanaboyina, C. M. Putman, R. D. Millán, and A. F. Frangi, "Efficient pipeline for image-based patient-specific analysis of cerebral aneurysm hemodynamics: Technique and sensitivity," *IEEE Trans. Med. Imag.*, vol. 24, no. 4, pp. 457–67, Apr. 2005.

[41] S. Bouix, K. Siddiqui, and A. Tannenbaum, "Flux driven automatic centerline extraction," *Med. Image Anal.*, vol. 9, pp. 1209–221, 2005.

[42] A. K. Jain, R. Duin, and J. Mao, "Statistical pattern recognition," *IEEE Trans. Pattern Anal. Mach. Intell.*, vol. 22, no. 1, pp. 4–37, Jan. 2000.

[43] R. Kohavi, "A study of cross-validation and bootstrap for accuracy estimation and model selection," in *Proc. 14th Int. Joint Conf. Artif. Intell. (IJCAI)*, C. Mellish, Ed., San Francisco, CA, 1995, pp. 1137–1143 [Online]. Available: citeseer.ist.psu.edu/kohavi95study.html

[44] N. Kassell and J. Torner, "Size of intracranial aneurysms," *Neurosurgery*, vol. 12, pp. 291–297, 1983.

[45] D. O. Wiebers, J. P. Whisnant, T. M. J. Sundt, and W. M. O'Fallon, "Intracranial aneurysms size and potencial for rupture," *J. Neurosurg. Lett.*, vol. 67, p. 476, 1987.

[46] K. Kataoka, M. Taneda, T. Asai, A. Kinoshita, M. Ito, and R. Kuroda, "Structural fragility and inflammatory response of ruptured cerebral aneurysms. A comparative study between ruptured and unruptured cerebral aneurysms," *Stroke*, vol. 30, pp. 1396–1401, 1999.

[47] K. Kataoka, M. Taneda, T. Asai, and Y. Yamada, "Difference in nature of rupture and unruptured cerebral aneurysms," *Lancet (Lett.)*, vol. 355, p. 203, 2000.

[48] M. A. Eisenberg and L. E. Malvern, "On finite element integration in natural coordinates," *Int. J. Numer. Methods Eng.*, vol. 7, pp. 574–575, 1973.